

## AN INVESTIGATION INTO TWO ALTERNATIVE APPROACHES FOR THE IDENTIFICATION OF SFD BEARINGS FOR AEROENGINE ANALYSIS

**Keir Groves**

School of Mechanical, Aerospace and Civil  
Engineering, University of Manchester  
Manchester, UK

**Philip Bonello**

School of Mechanical, Aerospace and Civil  
Engineering, University of Manchester  
Manchester, UK

### ABSTRACT

Identification techniques provide a means of efficiently implementing complex nonlinear bearing models in practical turbomachinery applications. This paper considers both identification from an advanced numerical model and identification from experimental tests. Identification from numerical models is essential at the design stage, where rapid simulation of the dynamic performance of a variety of designs is required. Experimental identification is useful to capture effects that are difficult to model (e.g. geometric imperfections, compressibility and its effect on cavitation). With regard to identification from a numerical model, it was shown in a previous paper that the numerical solution of the incompressible Reynolds equation may be replicated using Chebyshev polynomial fits. Tests were performed on a simple rotor-bearing configuration incorporating an advanced numerical bearing model. The identified model was found to be able to match the accuracy of the numerical solution to the Reynolds equation while requiring a fraction of the computation time. In the present work the SFD identification scheme is applied to a realistically-sized representative whole-aeroengine model. It is shown that using recently introduced nonlinear solvers combined with the identified high accuracy bearing models it is possible to run full engine rotor-dynamic simulations, in both the time and frequency domains, at a fraction of the previous computational cost. One major drawback of the Chebyshev technique is that it is not amenable to experimental identification of actual bearings. For this reason, a second identification approach, involving the use of neural networks, is considered in this paper. A test rig that enables empirical identification of SFD forces has been constructed and details of the building and operation of the test rig is presented. The method used to ascertain the training data

required by the neural network identification scheme, is also described.

### 1 INTRODUCTION

Squeeze film dampers (SFDs) are frequently used for attenuating vibration and transmitted forces in rotating machinery. An SFD comprises a thin pressurised oil film within the annular clearance between the non-rotating outer race of a rolling-element bearing (the SFD journal) and its housing. Its compact size and robustness make it commonplace within modern aircraft gas turbine engines. However, in order to ascertain smooth running, the deployment of these bearings in such machinery necessitates the ability to perform unbalance response analysis that takes account of the bearing nonlinearity. The challenges faced by the analyst are twofold: (a) the complexity of the structural dynamics of two/three-spool aeroengines; (b) the reliability of the model used to represent the SFDs. Recent developments by the authors in the area of identification techniques [1] (addressing challenge (b)), alongside advances in the computational speed of nonlinear whole-engine solvers of Bonello and Hai [2, 3] (addressing challenge (a)), have opened the possibility of using advanced numerical SFD models in whole-engine simulations, where previously such analysis was computationally prohibitive.

The nonlinear solvers used to calculate the unbalance response work either in the time domain or in the frequency domain. Time domain solvers progress forward in time until a steady-state response is obtained that may not necessarily be periodic. Frequency domain solvers are inherently much faster since they extract steady-state solutions that are assumed to be periodic of given fundamental frequency. Previous studies e.g. [3] have illustrated the benefit of a computational facility that takes advantage of the relative merits of both time and

frequency domain methods through an integrated approach that makes effective use of both. Prior to the research in [2, 3], such time/frequency domain calculations on realistic aeroengine models were prohibitive due to the large number of assembly modes that need to be considered. This problem has been overcome by the novel Impulsive Receptance Method (IRM) and the Receptance Harmonic Balance Method (RHBM), which efficiently solve the nonlinear problem in the time and frequency domains respectively [2, 3]. The IRM is an implicit integration algorithm. Its equations relate the instantaneous relative displacements and velocities at the nonlinear elements (SFDs) with the motion-dependent excitations (SFD forces, gyroscopic moments) and other excitations (unbalance, distributed rotor weight) acting on the linear part of the system. Hence, unlike conventional implicit integrators, the IRM's computational efficiency is largely immune to the number of modes since the number of equations to be solved at each time step is dependent only on the number of SFDs [2]. The RHBM is the frequency-domain counterpart of the IRM. It is similarly immune to the number of modes since it makes use of frequency response functions ('receptances') to relate the harmonics of the relative displacements at the SFDs with the corresponding harmonics of the excitations (motion-dependent and otherwise) acting on the linear part of the system [3]. The unknowns to be solved for are the harmonics of the relative displacements at the SFDs. Since the SFD forces are known nonlinear functions of the relative displacements and velocities, the harmonics of the SFD forces are determined through a Fourier analysis of their time histories for an assumed solution. This allows solution by iteration [3].

The reliability of the response prediction clearly hinges on the reliability of the model used for the SFDs. Moreover, like conventional methods, these new methods still require a number of SFD force computations per time step (IRM) or iteration (RHBM). In the case of RHBM, one iteration requires the calculation of the SFD forces at each of an adequate number of time points over the period of vibration in order to obtain their Fourier coefficients. The iterative process also requires a Jacobian matrix that is obtained through repeated calculation of these Fourier coefficients. The SFD model can cripple a time/frequency domain solver unless the SFD forces are rapidly computed. In summary, the speed/reliability of the unbalance response solution is wholly dependent on the speed/reliability of the SFD model

To enable rapid computation of SFD forces, SFD models based on one dimensional approximations of the Reynolds lubrication equation are commonplace within industry and the literature [2-4]. Such one-dimensional analytical solutions are achieved by assuming that pressure gradients in one direction, either circumferential or axial, are negligible and are respectively named short and long bearing solutions. In the literature there are many variants of the long and short bearing approximations [4, 5]. The most prominent of these variants involves the combination of the short and long pressure solutions through an empirical 'end-leakage factor'  $\lambda$  that accounts for the degree of end-sealing [5, 6]. This model is

popular with industry and was used recently for whole-engine analysis with 5 SFDs using IRM and RHBM [7]. As stated in [1], the factor  $\lambda$  can only be related to the parameters of a given bearing when it is hosted in a given experimental setup. Attempts to theoretically relate it to the SFD parameters have proved unsuccessful [5]. Moreover, this  $\lambda$ -model cannot account for the effect of the groove and feed-ports.

A numerical scheme such as finite difference (FD) [8] or finite element (FE) [9] is required if the Reynolds equation is to be solved in its full two-dimensional form with realistic boundary conditions. The use of such a numerical scheme within a time/frequency domain solver is computationally unattractive, even prohibitive for large engine simulations. This leads to the work of a previous paper [1], wherein a novel identification technique was presented that provides a rapid means for FD models to be deployed. Boundary conditions were developed to allow the SFD model to include any combination of end-plate seals, grooves and feed-pipes. The technique has benefit over previous similar works of Rodrigues et al. [10] and Chen et al. [11] since no assumption was made about the range of input variables, the cavitation pressure or the axial symmetry of the pressure boundary conditions.

The technique introduced in [1] was only tested on a simple test rig. In Section 2 of this paper, the first whole-aeroengine analysis is performed using an advanced two-dimensional numerical bearing model, which can account for an arbitrary number of non-axisymmetric boundary conditions. The engine-model analysed is a twin-spool 5-SFD engine that was previously analysed in [2, 3] using the  $\lambda$ -model. The identification technique introduced in the current work is an even more efficient version of the identified FD model presented in [1].

Despite the significant developments regarding the identification of advanced theoretical models in [1], there are still inherent limitations. The use of the incompressible Reynolds equation means that the effects of compressibility due to air entrainment are not accounted for. Variable cavitation pressure is often observed in experiments [5, 12], suggesting that air entrainment and therefore cavitation is dependent upon the bearing dynamics. Although attempts have been made to account for compressibility of the fluid film e.g. [13, 14], these have always come at the expense of other significant effects, namely the prescription of realistic boundary conditions. Moreover, a theoretical model may fail to account for geometric imperfections that exist within the SFD assembly. Due to the scale of a typical SFD, deviation from theoretical geometry is highly likely; such imperfections can have a significant effect on SFD behaviour e.g. seal gap dimension and clearance shape.

For the reasons given in the previous paragraph, identification from empirical data is also considered. Section 3 of this paper gives details of a test rig that is capable of measuring SFD forces and relative motion across the film. Using a sophisticated identification technique it is possible to 'learn' the empirical relationship between SFD force and

relative journal motion. This technique provides an SFD model that is individual to the particular SFD. The model will intrinsically contain all complexities of the SFD force relationship and account for any imperfections within the SFD geometry. Once identified, the SFD model may be applied to any rotor-dynamic system, enabling the realisation of a truly realistic response.

Previous works e.g. [15, 16] have performed empirical identification on rotordynamic systems. However, works involving SFDs (e.g. [15]) are limited to the use of linearised force coefficients to compute SFD forces. The linear assumption is only valid for small amplitude vibrations about a fixed location; thus limiting them to highly idealised conditions which are unsuitable for realistic engines. Medina and Parada [16] use a neural network based scheme to identify the open loop response of an active magnetic bearing. A NNARX (neural network autoregressive external input model) neural network with multilayer perceptron topology was used to relate amplifier current demand to shaft position information, while operating in closed loop with a plant controller. The system was trained using data generated by adding a chirp signal to the output of the plant controller. Identification was successfully validated using unbalance applied to the rotating shaft. Despite successful identification, applications of the technique are somewhat limited to use in controller design.

## 2 TWIN SPOOL ENGINE MODEL WITH THEORETICAL IDENTIFICATION

In the present section the first full aeroengine analysis that includes two-dimensional SFD models with advanced geometric boundary conditions is presented. The analysis considers the same representative twin-spool aeroengine, from a leading manufacturer, used in [2, 3]. The schematic layout of this engine is reproduced in Figure 1. As can be seen from Figure 1, a parallel retainer spring ('squirrel cage') is only used with one SFD at the end of each rotor for axial location.

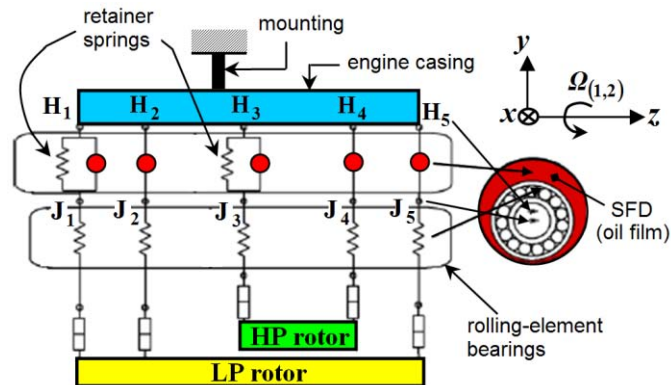


Figure 1: Schematic of a typical twin-spool engine [3]

### 2.1 Rotor-dynamic Solution Procedure

The reader is referred to references [2, 3] for a full description of the workings of the IRM and RHBM solvers. The complete nonlinear rotor-dynamic assembly is regarded as

a non-rotating linear part acted on by 'external' excitation (comprising the unbalance, the distributed rotor weight, the gyroscopic effect and the SFD forces). By "linear part" is meant the structure left after all SFDs in the schematic of Fig. 1 are replaced by 'gaps'. A realistically-sized finite-element (FE) model of the linear part (including the casing) was provided by the engine manufacturer.

The IRM and RHBM require a preliminary one-off eigenvalue analysis of the undamped linear part at zero rotational speed. The modal displacements (eigenvectors) were then extracted at the degrees of freedom of interest (e.g. those at the SFD positions) and used as input data for the IRM and RHBM solvers to calculate the unbalance response of the complete nonlinear rotating system.

For the case analysed in this paper the unbalance was restricted to the LP rotor only (corresponding to the single frequency unbalance (SFU) excitation case analysed in [3]). The unbalance was applied at two locations, one at each end of the LP rotor, to simulate unbalance in the fan and the LP turbine. The unbalances were in-phase and of magnitude 6.3 kgmm. Reference [3] provides a figure detailing the relative axial positions of the SFDs and the unbalance locations, as well as the distribution of the weights of the two rotors. The gyroscopic effect was discretised at 7 points on the LP rotor and 12 points on the high-pressure (HP) rotor.

The bearing housings were assumed to be perfectly aligned with each other prior to rotor assembly. As in [2, 3], the SFDs considered for this study were single-land and ended with oil of viscosity 0.0049 Nsm<sup>-2</sup> at a pressure of 3 bar (gauge). The overall bearing dimensions were the same as those used in [3]: the bearing diameters and radial clearances were typically 200 mm, 0.1 mm respectively and the land lengths ranged from 16 to 34 mm. Those dimensions of the SFD features that were not modeled in the simplified bearing model used in [2, 3] (namely the groove, the end-seal and the feed-ports) were assumed by the authors and do not correspond to any particular bearing used by the manufacturer.

The nonlinear analysis was performed for a fixed speed ratio  $\Omega_{(2)}/\Omega_{(1)}=1.2$  where  $\Omega_{(1)}$ ,  $\Omega_{(2)}$  are the speeds of the LP, HP rotors respectively. All 934 modes of the linear part over the range 0-1kHz were included in the nonlinear analysis due to high shaft speeds and harmonics in the response. In the case of the IRM, the number of equations solved at each time step is 20 [1]. In the case of the RHBM since the case considered is SFU, the fundamental frequency of the response was taken to be synchronous with the speed of the unbalanced shaft ( $\Omega_{(1)}$ ). As in [3], eight harmonics of this frequency were considered and so the total number of unknown Fourier coefficients was 174. A predictor-corrector continuation scheme was used to advance the RHBM solution process over a range of speeds tracing out a 'speed-response' curve [3]. The initial approximation ('predictor') to the Newton-Raphson solver at an attempted solution point on the speed response curve was estimated from the previous solution points. The initial approximation to the *first* solution point (only) was provided by the Fourier coefficients of a time-domain solution.

All simulations were performed in Matlab on a standard desktop pc with Intel® Pentium® D CPU 3GHz processor.

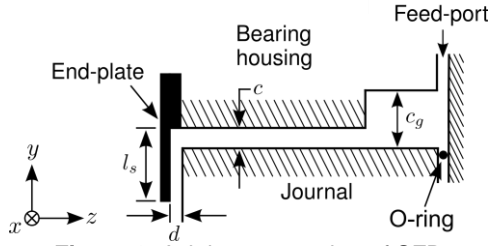


Figure 2: Axial cross-section of SFD

## 2.2 SFD models

The SFDs used in the engine are end-plate sealed, end-fed bearings as per Figure 2. The SFD modeling techniques are taken from [1], where detailed information may be found. However, a brief description is given below. Fluid film inertia effects are neglected in the SFD model as the identification technique, in its present state, does not lend itself to the inclusion of the extra acceleration variables.

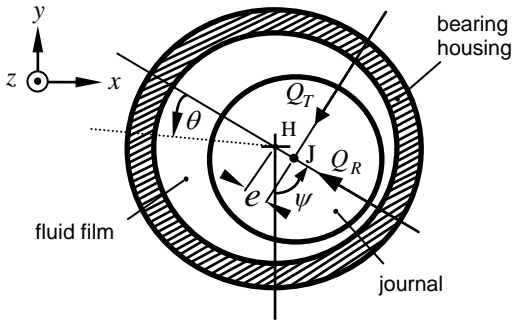


Figure 3: Polar coordinate system

With reference to Figure 3, the instantaneous pressure distribution  $p(z, \theta)$  is given by the solution to the incompressible Reynolds equation [17]:

$$\frac{1}{R^2} \frac{\partial}{\partial \theta} \left\{ h^3 \left( \frac{\partial p}{\partial \theta} \right) \right\} + h^3 \frac{\partial^2 p}{\partial z^2} = 12\mu(e\dot{\psi} \sin\theta + \dot{e}\cos\theta) \quad (1)$$

.... where  $h = c + e\cos\theta$ . The radial and tangential SFD forces  $Q_{R,T}$  are then given by:

$$\begin{bmatrix} Q_R \\ Q_T \end{bmatrix} = -2RL \int_0^{L+L_g} \int_0^{2\pi} p_t(z, \theta) \begin{bmatrix} \cos\theta \\ \sin\theta \end{bmatrix} dz d\theta \quad (2)$$

... where  $p_t(z, \theta)$  is a pressure distribution that is truncated to account for oil film rupture due to cavitation:

$$p_t(z, \theta) = \begin{cases} p(z, \theta) & \text{if } p(z, \theta) > p_{cav} \\ p_{cav} & \text{if } p(z, \theta) \leq p_{cav} \end{cases} \quad (3)$$

In this research, the cavitation pressure  $p_{cav}$  is set to -101.325 kPa (absolute zero) as recommended in [13, 18] and used in [1-3].

The Reynolds equation is solved by converting partial derivatives into central difference formulas and using Castelli's column method [8] to solve for a grid of pressures  $p_{i,j}$  over the SFD land where  $j$  refers to node locations in the  $\theta$  direction and  $i$  refers to locations in the  $z$  direction. The FD solution is then identified using Chebyshev polynomials. Using the technique introduced in [1], the identification is performed upon the static and dynamic components of each mesh point pressure:

$$p_{i,j} = p_{dyn_{i,j}}(e, \dot{e}, \dot{\psi}, \psi) + p_{stat_{i,j}}(e, \psi) \quad (4)$$

This allows the addition of arbitrary boundary conditions cavitation pressure while maintaining the benefits of the reduction technique of Chen et al. [9]. This reduction technique exchanges  $\dot{e}$  and  $\dot{\psi}$  in the first term of (4) for a single variable  $q_{1/2}$  with limits of  $\pm 1$ . The reader is referred in [1] for the details of this manipulation.

Two alternative SFD models are identified in this analysis. The first SFD model is termed the deep groove model, it has moderate end-plate sealing and pressure at the groove is assumed to be constant. The end-plate seal boundary condition assumes a constant pressure gradient within the seal and constant outlet pressure. By performing a volume flow balance at the seal entrance it may be shown that considering the pressure mesh  $p_{i,j}$ :

$$\frac{1}{12\mu} \left( \frac{dp}{dz} \Big|_{1,j} \right)_a (h_j)_a^3 = \frac{1}{12\mu} \left( \frac{p_{out} - (p_{1,j})_a}{l_s} \right) d^3 \quad (5)$$

The second model maintains moderate sealing and accounts for the added damping effect of the groove as well as the hydrodynamics of the feed-ports; this model is termed the feed-port model. To model the feed-groove an extra land is added onto the existing model. The relationship between the land and groove is established by continuity of flow in the  $z$  direction at the boundary between them. Equating flow rates gives

$$-\frac{1}{12\mu} \left( \frac{dp}{dz} \Big|_{N_i,j} \right)_a (h_j)_a^3 = -\frac{1}{12\mu} \left( \frac{dp}{dz} \Big|_{1,j} \right)_b (h_j)_b^3 \quad (6)$$

The feed-port boundary condition is achieved by implementing a pipe flow relationship [19], the volume flow rate is expressed as a function of the variable pressure at the feed-port outlet and the constant supply pressure  $p_s$  in the pipe leading to the feed-port :

$$v_f = \frac{1}{8} \frac{A_h \{ p_s - (p_{N_i,j})_b \}}{\pi \mu l_p} \quad (7)$$

Once more, by performing a volume flow balance at the port the boundary condition may be obtained.

In the present work, the polynomial computation routine used in [1] is greatly improved by reducing the number of redundant calculations performed. The pressure function is identified for a grid of nodes covering the bearing land and is a

function of 1 to 3 variables, dependent upon the component of pressure being considered (static or dynamic) and the axial symmetry of the boundary conditions. A Chebyshev polynomial of degree  $r$  is defined as  $T_r(x) = \cos(r \arccos(x))$ , for  $-1 \leq x \leq 1$  and  $r = 0, 1, 2, \dots, m$ . Letting  $f_{fit}(e, \psi)$  denote the Chebyshev polynomial fit of the function  $f(e, \psi)$  with two dependant variables, then:

$$f_{fit}(e, \psi) = \sum_{r=0}^m \sum_{s=0}^n C_{r,s} T_r(\tilde{e}) T_s(\tilde{\psi}) \quad (8)$$

where,  $C_{r,s}$  are the coefficients that may be determined by invoking the orthogonality of the polynomials [10],  $\tilde{e}$  and  $\tilde{\psi}$  are  $e$  and  $\psi$  normalised over the range  $\pm 1$ :

$$\tilde{e} = 2(e - 1/2(e_{max} + e_{min})) / (e_{max} - e_{min}) \quad (9)$$

...similarly for  $\tilde{\psi}$ . For efficiency within Matlab®, computation of the pressure grid is performed as a matrix operation. Although immensely faster than computing sequentially, it has the drawback that at each pressure location the same number of polynomial coefficients  $C$  must be used. This causes much redundant processing since high order polynomials are only necessary at more central locations within the grid. At locations away from the centre of the pressure grid, high order polynomial fits result in a large amount of near zero coefficients that are included in the pressure computation. To reduce computations on near zero polynomial coefficients, while retaining the benefit of parallel computation, a reduction technique has been implemented. The technique identifies regions within the pressure grid that require a similar number of coefficients and arranges them into smaller matrices while a vector of their origin is recorded. Splitting the calculation into three segments was found to give the best balance between time saving from reduction of null coefficients and time cost from the system working sequentially combined with the re-indexing process. The reduced system can perform forward computation in approximately half the time with no loss of accuracy.

### 2.3 Engine analysis with deep groove bearing model

Two key tests were performed on the engine model. First, a transient analysis was performed using a combination of solvers and bearing models to demonstrate agreement between the different methods and to profile the time savings that can be achieved using the identification technique described in 2.2 and the IRM time domain solver of [2]. Second, steady-state speed responses were performed using the RHBM solution method of [3] to demonstrate the computational savings that may be achieved by using identified bearing models in frequency domain analysis. In the following discussion, the identified SFD model is referred to as the 'FD-Chebyshev' SFD model.

The transient analysis was performed over 10 LP rotor revolutions from default initial conditions (corresponding to zero relative displacements and velocities at each SFD). The low pressure (LP) and high pressure (HP) rotor speeds were

10,000 and 12,000 rev/min, respectively. The SFD model used a seal gap ratio  $d/c$  of 0.5 with a seal length of 3mm. The pressure grid used 101 nodes on the  $\theta$  axis and 51 nodes in the  $z$  axis. In testing, convergence of the pressure mesh was observed at 61 nodes on the  $\theta$  axis and 31 nodes in the  $z$  axis. The highest degree of Chebyshev polynomial used for each variable is shown in Table 1. The analysis was performed for three cases: (a) using the IRM solver and the (unidentified) FD SFD model; (b) using the IRM solver with the FD-Chebyshev SFD model and (c) using a conventional implicit integrator (i.e. Matlab®'s *ode23s*© routine) with the FD-Chebyshev SFD model. This latter case was included to confirm the robustness of the IRM. Figure 4 shows the relative displacement (i.e. journal relative to housing), relative velocity and force orbits obtained from the LP-rear bearing (SFD no.5 in Figure 1) for the IRM-FD case. Plots from the other cases have been omitted as the orbits are indistinguishable. The LP-rear bearing was chosen to be presented as it is the furthest from the retainer spring and will therefore have the most nonlinear response. To compute the IRM-FD response took 11000 s; using Matlab®'s *ode23s*© with FD-Chebyshev took 9600 s while using IRM-FD-Chebyshev took only 350 s. These results clearly show that the combined use of the IRM technique and the FD-Chebyshev can drastically reduce computation times.

Pressure function	Variable	Degree of polynomial
for $P_{dyn,i,j}$	$e$	25
	$q_{1/2}$	1
for $P_{stat,i,j}$	$e$	4

**Table 1:** Highest degree of polynomials used to perform fit for the deep groove bearing model

RHBM speed response curves were obtained using both the FD bearing model and the FD-Chebyshev bearing model over an LP rotor speed range of 150 to 200 rev/s. Figure 5 shows the orbit amplitude obtained from the LP-rear bearing in the  $y$  direction, computed using the RHBM. The amplitudes were also checked by IRM at discrete speeds. From the plot, near perfect agreement is clear between FD, Chebyshev and IRM, equally excellent agreement was observed at the other four bearings. Figure 6 presents the times taken to produce the orbits for both the Chebyshev and FD bearing models. It is quite clear that the Chebyshev technique can accurately mimic a FD model in under 10% of the time.

### 2.4 Engine analysis with feed-port bearing model

The previous section verified the validity of using Chebyshev identification to implement FD models. In the present section the same steady-state analysis of section 2.3 is performed with the more advanced feed-port model that includes the groove as a damper land and models the hydrodynamics of the oil-feed arrangement. The inclusion of feed-ports increases the dimension of the pressure function input space as pressure becomes a function of  $\psi$  as well as  $e$ ,  $\dot{e}$  and  $\dot{\psi}$ . This causes the dimension of the polynomial

coefficient matrices to rise by 1 in accordance. The highest degree of Chebyshev polynomial used for each variable is shown in Table 2. For the FD scheme to function accurately, the node spacing must be equal throughout the pressure grid. Since both land length and groove length are fixed, careful selection of the number of nodes is necessary to ensure equal node spacing. The number of nodes in the  $z$  direction was always above 30 while greater than 60 nodes was maintained in the  $\theta$  direction as testing revealed that force computation accuracy degrades below these values. The groove  $c_g$  was considered to be 1 mm deep with a length of 4 mm and the oil-feed is modeled as three equispaced feed-ports of diameter 1 mm and length 20 mm.

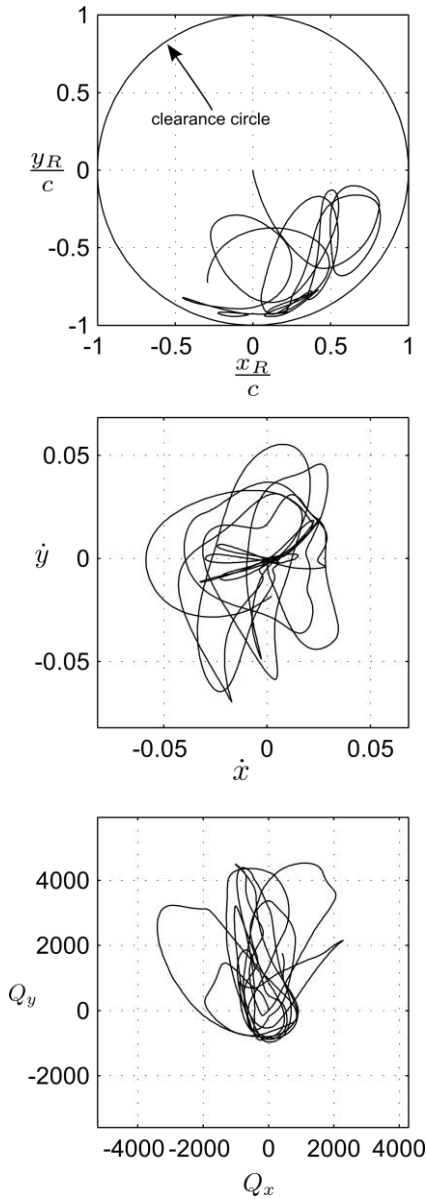


Figure 4: Transient response of SFD 5 using the IRM solver and FD SFD model

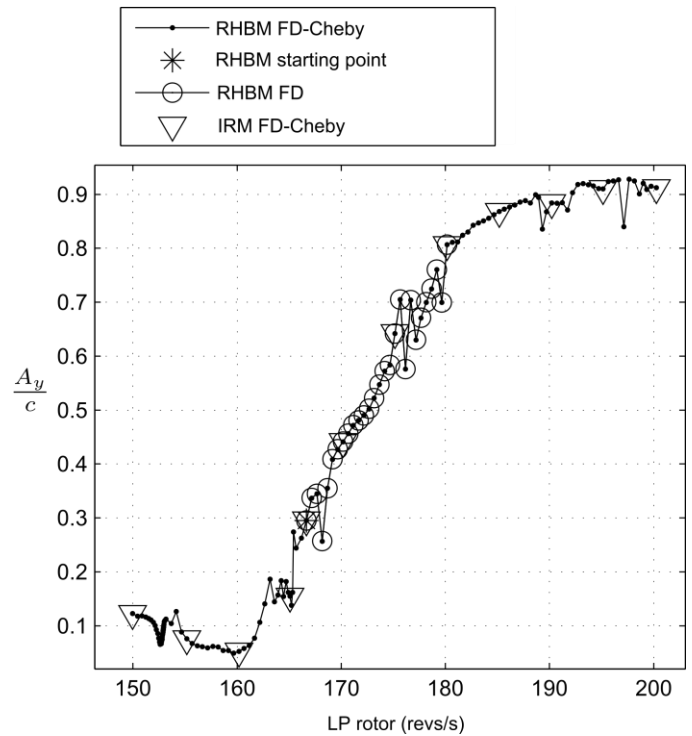


Figure 5: Speed response curves of the  $y$  relative displacement at SFD 5 (vertical axis gives half-peak-to-peak amplitude normalised by the radial clearance)

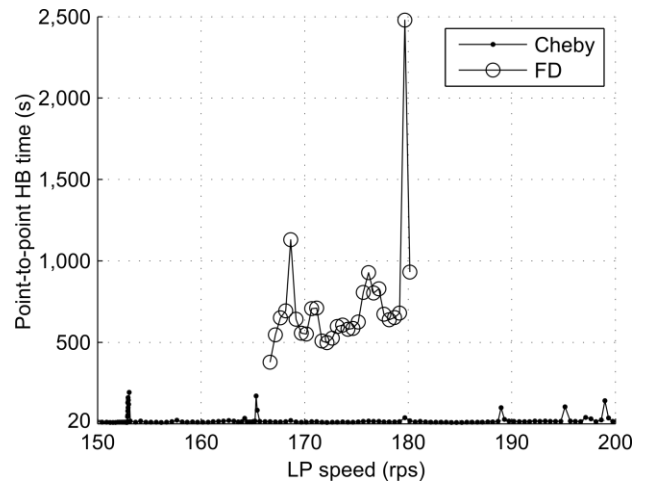
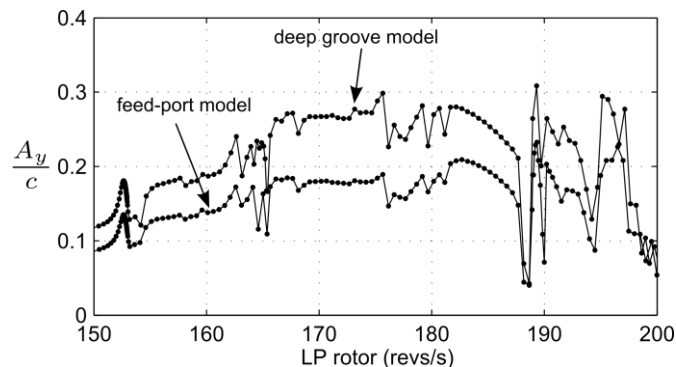


Figure 6: Chebyshev vs. FD with RHBM speed control-control continuation

Pressure function	Variable	Degree of polynomial
for $p_{dyn i,j}$	$e$	25
	$q_{1/2}$	1
	$\psi$	7
for $p_{stat i,j}$	$e$	4
	$\psi$	4

Table 2: Highest degree of polynomials used to perform fit for the feed-port bearing model

Figure 7 shows the orbit amplitude obtained from SFD 1, computed with FD-Chebyshev and RHBM. Both the response using the deep groove model and the feed-port model are plotted. The plot clearly shows the increased damping introduced by the shallow groove over the complete speed range. This is attributed to the fact that in the feed-port model the groove is treated as an extra land, without a fixed boundary pressure at the feed end. Added damping was observed at all of the bearing locations but was found to be most pronounced at SDF no. 1.



**Figure 7:** y-relative displacement amplitudes calculated for SFD 1 computed using RHBM for the deep groove and feed-port model (vertical axis gives half-peak-to-peak amplitude normalised by the radial clearance)

### 3 EMPIRICAL SFD IDENTIFICATION

Using a purpose-built test rig, SFD forces and the hydrodynamic motion that acts to create them may be measured and used to train a neural network. The end goal is to deploy such an identified bearing model within an all-encompassing engine model, as performed in section 2. At this stage however, identified SFD forces are compared to experimental readings and theory as a basis for future work.

#### 3.1 The test rig

The test rig of figure 8 was converted from a rotating rig to a specially designed identification setup. The test rig consists of a heavy rotor with a self-aligning bearing support at the right hand end and a single bar spring at the left. Also at the left hand end is an SFD that is flexibly supported. The rotor is prevented from rotating and the excitation force is supplied by a pair of orthogonal shakers that can accept custom input signals. The bar spring is relatively flexible as it is designed to hold the static load of the rotor while allowing free movement of the SFD journal within the housing. The linear subsystem may be separated into its horizontal and vertical components. A point mass model of the system is presented in figure 9. Impact testing was performed upon both the housing and the journal and it was confirmed that a point mass model is applicable over the frequency range considered. The effective mass of the rotor at the SFD is 21.27 kg while the stiffness of the bar ( $k_J$ ) is 305 kN/m in both the horizontal and vertical directions. The effective housing mass is 4.369 kg in the horizontal direction and 4.325 kg in the vertical and the housing stiffness values ( $k_H$ ) are 601 kN/m and 592 kN/m respectively. The SFD in the test rig is a lightly sealed two-

land bearing with a relatively deep groove where oil supply is provided through 3 equispaced feed-ports in the bearing housing. The SFD parameters are presented in Table 3.

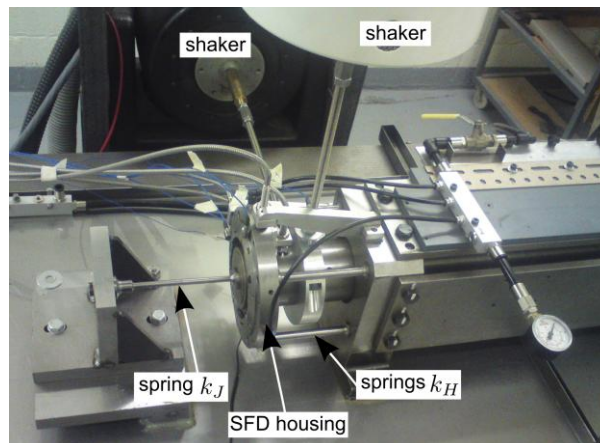


**Figure 8:** Photo of the test rig converted for identification

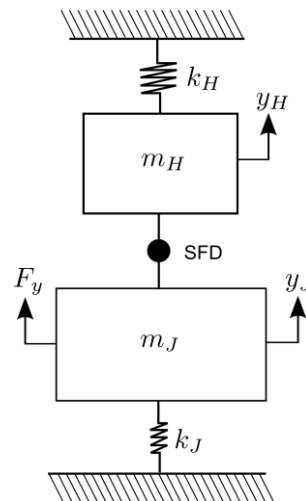


**Figure 9:** Point mass model of the test rig

Journal radius	69.85 mm
Radial clearance	0.90 mm
Land length	6.23 mm
Groove width	7.42 mm
Groove depth	2.03 mm
Seal gap	0.5 mm
Seal length	3.15 mm
Oil viscosity	0.0049 Pa s
Feed-port diameter	1.5 mm
Feed-port length	25 mm
Feed pressure	80 kPa

**Table 3:** SFD parameters

Relative displacement across the film is measured by a pair of displacement probes attached to the SFD housing. The absolute displacement of the housing is measured by another pair of probes attached to a rigid frame. Accelerometers are

attached to the journal and housing and the force applied to the test rig is measured by force gauges fixed in the shaker stingers. To perform identification on the SFD, instantaneous relative displacement and velocity in two directions must be recorded, alongside the cross-coupled SFD forces. While relative displacement is measured directly by the probes, relative velocities are computed in two alternative ways. Firstly by differentiation of the filtered displacement signal, secondly by the integration of the relative acceleration that is ascertained by subtracting the housing acceleration from that of the journal. Computation of the SFD force is also performed in two ways to ensure that measurement is correct. With reference to figure 9, the SFD force is computed as:

$$Q_y^H = m_H \ddot{y}_H + k_H y_H \quad (10)$$

...and also as:

$$Q_y^J = m_J \ddot{y}_J + k_J y_J - F_y \quad (11)$$

### 3.2 The neural network

Empirical identification is much better suited to the use of a backpropagation trained neural network identification scheme than Chebyshev polynomial approximations. The nature of the backpropagation scheme means that a certain degree of noise can be tolerated in the training data. This is due to the fact that the network weights and biases are only modified to *reduce* the network error for an individual training vector and not fully eliminate it. Conversely to Chebyshev polynomials, a neural network can be trained on any data that is available. This means that the training data locations and shape of the input space is not prescribed by the network; the network adapts to the data it is fed. Since it is not possible to experimentally implement the reduction technique used in [1] the inclusion of 4 input variables is necessary. This is another reason why the use of Chebyshev polynomials is unsuitable. While Chebyshev identification for greater than 3 input variables is possible, the procedure becomes cumbersome [10].

Neural network training and implementation was performed using the Matlab® neural network toolbox. A feed-forward network with 4 layers was used. The input layer had 4 neurons while the two hidden layers both had 8 neurons and the output layer had 2 neurons. All layers used hyperbolic tangent sigmoid transfer functions and all inputs and outputs were normalised. Training was performed using Levenberg-Marquardt optimization and was stopped by use of a validation data subset that comprised 20% of the initial training data. Inputs to the network were the displacements and velocities of the SFD journal relative to the housing,  $x_R$ ,  $y_R$ ,  $\dot{x}_R$  and  $\dot{y}_R$ , while the outputs were  $Q_x$  and  $Q_y$ .

The range and quality of data is a key factor in achieving good identification. Since the data is empirically obtained it is not possible to prescribe data locations within the input space. Instead, a range of forcing functions must be selected that induce the desired coverage of the input space. It is also of key importance that the data, upon which the network is trained, is significantly different in nature from test data. For these

reasons the training data was obtained by applying band limited random signals to the shakers of varying amplitude and frequency content. Table 4 presents the various signal properties used in the creation of training data. For each random signal, 60 seconds of data was taken in 10 second blocks, the data was sampled at 3,200 Hz. The raw data was filtered to remove excess noise and verified by testing agreement between the readings from different sensors. The data was processed to compute velocities  $\dot{x}_R$  and  $\dot{y}_R$  and SFD forces  $Q_x$  and  $Q_y$ . Once processed, the data was re-sampled at 640 Hz to achieve a significant difference between consecutive data points. Finally, the data was jumbled to prevent similar training pairs being presented to the network successively. Training was performed 5 times and the network that achieved the lowest mean square error selected.

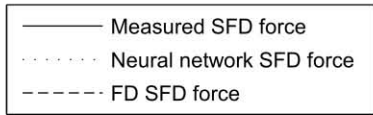
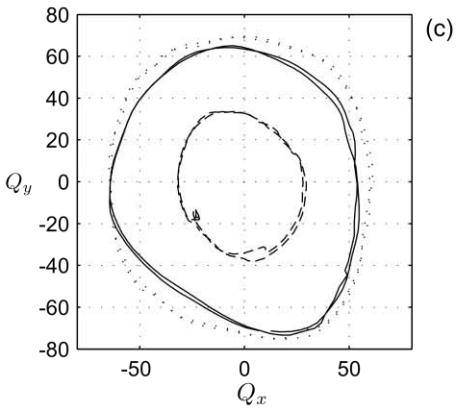
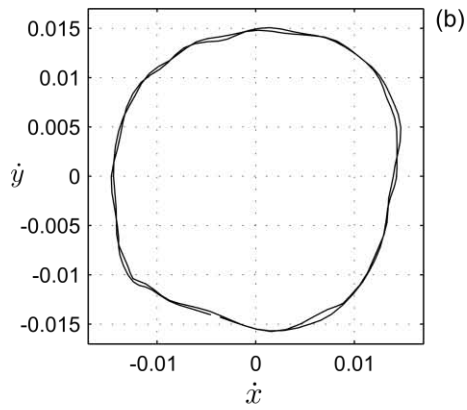
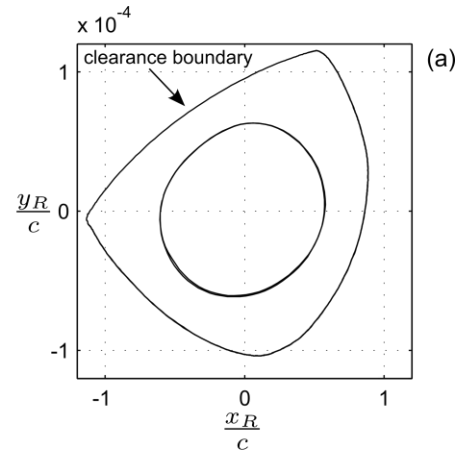
Force N(RMS)	Frequency content Hz
37	10-50
37	10-100
50	10-30
50	10-50
50	10-100
60	10-70
60	10-200

Table 4: Random force function parameters

### 3.3 Results

The network identification was tested by applying to the rotor orthogonal shaker forces that mimic the force from a rotating unbalance. Relative vibration across the film and the SFD forces were measured under steady-state conditions. The use of entirely different signals for training and validation ensures that the network has not simply learned to reproduce the data set but has learned the SFD input-output relationship. Figure 10 shows two revolutions of the steady-state orbit of the SFD when a shaker-generated rotating unbalance force of amplitude 80 N and frequency 40 Hz is applied to the rotor. Figure 10a,b show the displacement and velocity orbits respectively while 10c shows the SFD force obtained in three ways: (a) measured from the test rig using Eq. (11); (b) calculated using the trained neural network; (c) using the feed-port FD scheme of section 2, with the bearing parameters of table 3. Figure 11 presents the same three plots but using a force signal with amplitude 115 N and frequency 60 Hz.

The clearance boundary, although generally assumed to be circular, was found to be distorted. In view of the small radial clearance and the machining tolerances the assumption of a perfect circular boundary is somewhat idealised. This further supports the need for identification schemes and SFD models that are capable of accounting for non-axisymmetric boundary conditions.



**Figure 10:** Steady-state response of the test rig under circular force with 80 N amplitude and 40Hz frequency

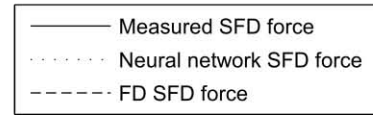
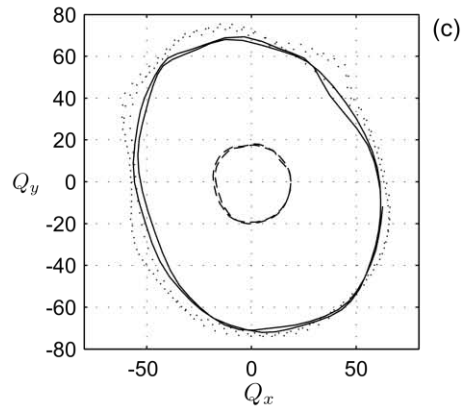
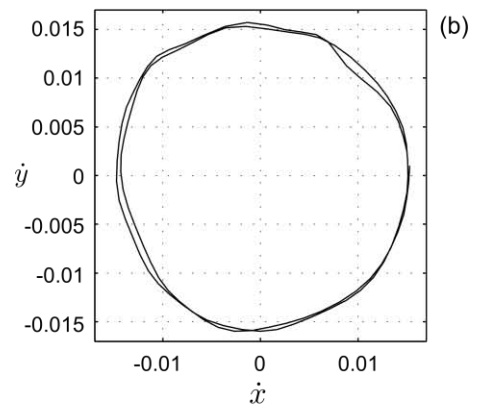
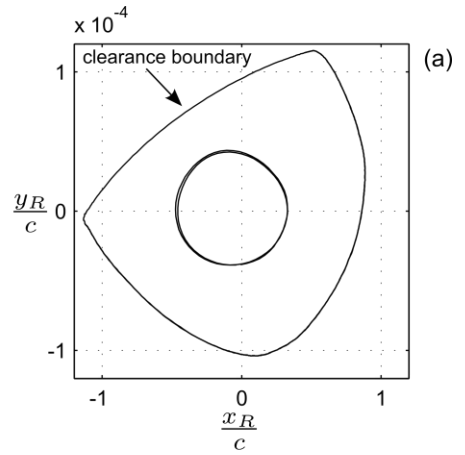


**Figure 11:** Steady-state response of the test rig under circular force with 115 N amplitude and 60Hz frequency

The results clearly show that the neural network has identified the SFD force function well. In Figure 10c the SFD force is slightly overestimated in general, but the shape and size of the orbit closely resembles the measured force. The theoretical FD-computed forces somewhat underestimate the SFD force and therefore the damping effect of the bearing. The results of figure 11c show a similar result. The identified SFD force orbit is slightly bigger than the measured orbit but in general the fit is very good. Again, the neural network model performs much better than the theoretical model as again the damping capability of the SFD is underestimated.

The slight discrepancy between measured and identified SFD forces in figures 10c and 11c may be attributed to the data used to train the neural network. The use of random excitation signals generated relative motion within the SFD with large variation of  $e$  and  $\dot{e}$  but somewhat lacking in  $\psi$  and  $\dot{\psi}$  variation. Therefore distribution of data within the training set may have adversely affected the training.

Negating the inclusion of acceleration terms in the identification means inertia of the fluid film may not be accounted for by the network. However, the identification manages to reproduce the SFD relationship well despite this omission. The implication of this is that inertia is not having a notable effect on force computation, therefore the underestimation of FD computed SFD forces is not due to the omission of fluid inertia effects. The cause may lie in the assumption that the SFD clearance is perfectly circular. It is quite clear from figures 10a and 11a that the clearance is irregular and this will have an impact upon the SFD forces.

#### 4 CONCLUSIONS

This paper has demonstrated the benefits that may be achieved in both computation time and accuracy by the use of identification techniques in SFD modeling. Time and frequency domain analyses on the nonlinear unbalance response of a whole-engine model were performed, for the first time, using a high accuracy two-dimensional bearing model that accounted for the effects of complex geometric boundary conditions. The ability of Chebyshev polynomial identification to reduce computation times by more than a factor of 10 while maintaining accuracy was demonstrated. The improved identification technique presented in this paper is shown to enable whole-engine analysis with advanced numerical SFD models within reasonable time frames on a standard desktop computer. The study also concluded that the use of a shallow groove in SFD design results in a significant reduction in vibration amplitude when compared to a deep groove model.

A novel identification technique based upon empirical data was then presented and preliminary investigations were shown to produce highly encouraging results. Previously, two-dimensional FD solutions to the Reynolds equation, with boundary conditions designed to replicate the hydrodynamic interaction of the fluid with the geometry of the land(s) and the feeding and sealing arrangement, were shown to be superior to approximate analytical solutions [1]. However, in the present paper it is shown that empirical neural network identification

can provide more reliable predictions than an advanced numerical model. The presented investigation into empirical identification, although instructive, performed only basic testing of the technique. Future work will focus on testing the ability of the technique in predicting the response of a test rig that incorporates an identified bearing as well as the inclusion of the empirically identified bearings in whole-engine analysis.

#### ACKNOWLEDGMENTS

The authors acknowledge the contribution of Dr Pham Minh Hai to the implementation of the rotor-dynamic codes used in section 2.

#### NOMENCLATURE

$A_h$	Area of the feed-port hole
$c$	Clearance of a centred SFD (m)
$C_i$	Chebyshev polynomial coefficients
$d$	Gap between sealing plate and journal (m)
$e$	Journal eccentricity (m)
$F$	Shaker force (N)
$h$	Squeeze film thickness (m)
$k$	Spring stiffness (N/m)
$l_s$	Effective length of end-plate seal (m)
$m$	Mass (kg)
$P$	Pressure (Pa)
$q$	Reduced form of $\dot{e}$ and $\dot{\psi}$
$Q$	Squeeze film force (N)
$R$	Radius of SFD journal (m)
$T_i$	The Chebyshev polynomials
$\theta$	Angular location (rad) see Figure 2
$\mu$	Dynamic viscosity (Pa s)
$\psi$	Attitude angle (rad)
$\Omega$	Rotor speed (rev/min)
$\dot{}$	differentiation with respect to time $t$
$()_R$	Relative property
$()_J$	Journal property
$()_H$	Housing property

#### REFERENCES

- [1] Groves, K. H., and Bonello, P., 2010, "Improved Identification of Squeeze-Film Damper Models for Aeroengine Vibration Analysis," *Tribology International*, 43 (9), pp. 1639-1649.
- [2] Hai, P. M., and Bonello, P., 2008, "An Impulsive Receptance Technique for the Time Domain Computation of the Vibration of a Whole Aero-Engine Model with Nonlinear Bearings," *Journal of Sound and Vibration*, 318 (3), pp. 592-605.
- [3] Bonello, P., and Minh Hai, P., 2009, "A Receptance Harmonic Balance Technique for the Computation of the Vibration of a Whole Aero-Engine Model with Nonlinear Bearings," *Journal of Sound and Vibration*, 324 (1-2), pp. 221-242.

- [4] Pietra, L. D., and Adiletta, G., 2002, "The Squeeze Film Damper over Four Decades of Investigations. Part I: Characteristics and Operating Features," *The Shock and Vibration Digest*, 34 (1), pp. 3-26.
- [5] Dede, M. M., Dogan, M., and Holmes, R., 1985, "The Damping Capacity of a Sealed Squeeze Film Bearing," *Transactions of the ASME, Journal of Tribology*, 107 pp. 411-418.
- [6] Holmes, R., and Dogan, M., 1985, "The Performance of a Sealed Squeeze-Film Bearing in a Flexible Support Structure," *Proceedings of the Institution of Mechanical Engineers, Part C: Journal of Mechanical Engineering Science*, 199 (1), pp. 1-9.
- [7] Bonello, P., and Hai, P. M., 2010, "Computational Studies of the Unbalance Response of a Whole Aero-Engine Model with Squeeze-Film Bearings," *Transactions of the ASME, Journal of Engineering for Gas Turbines and Power*, 132 pp. 032504.
- [8] Castelli, V., and Shapiro, W., 1967, "Improved Method for Numerical Solutions of the General Incompressible Fluid Film Lubrication Problem," *Transactions of the ASME, Journal of Lubrication Technology*, 89 pp. 211-218.
- [9] Jiangang, Y., Rui, G., and Yongwei, T., 2008, "Hybrid Radial Basis Function/Finite Element Modelling of Journal Bearing," *Tribology International*, 41 (12), pp. 1169-1175.
- [10] Rodrigues, F. A., Thouverez, F., Gibert, C., and Jezequel, L., 2003, "Chebyshev Polynomials Fits for Efficient Analysis of Finite Length Squeeze Film Damped Rotors," *Transactions of the ASME, Journal of Engineering for Gas Turbines and Power*, 125 (1), pp. 175-183.
- [11] Chen, Z., Jiao, Y., Xia, S., Huang, W., Zhang, Z., and Kirk, R. G., 2002, "An Efficient Calculation Method of Nonlinear Fluid Film Forces in Journal Bearing," *STLE Tribology Transactions*, 45 (3), pp. 324-329.
- [12] Holmes, R., and Dogan, M., 1982, "Investigation of a Rotor Bearing Assembly Incorporating a Squeeze-Film Damper Bearing," *Proceedings of the Institution of Mechanical Engineers, Part G: Journal of Aerospace Engineering*, 24 (3), pp. 129-137.
- [13] Feng, N. S., and Hahn, E. J., 1987, "Effects of Gas Entrainment on Squeeze Film Damper Performance," *Transactions of the ASME, Journal of Tribology*, 109 (1), pp. 149-154.
- [14] Levesley, M. C., and Priest, M., 2008, "A Bubbly Oil-Lubricated Squeeze Film Damper. Part 1: A Finite-Element Model," *Proceedings of the Institution of Mechanical Engineers, Part C: Journal of Mechanical Engineering Science*, 222 (11), pp. 2191-2201.
- [15] Kim, Y. H., Yang, B. S., and Tan, A. C. C., 2007, "Bearing Parameter Identification of Rotor-Bearing System Using Clustering-Based Hybrid Evolutionary Algorithm," *Structural and Multidisciplinary Optimization*, 33 (6), pp. 493-506.
- [16] Medina, J., Parada, M., Guzman, V., Medina, L., and Díaz, S., 2004, "A Neural Network-Based Closed Loop Identification of a Magnetic Bearings System," *Proceedings of ASME Turbo Expo, GT2004-53103* pp. 593-598.
- [17] Cameron, A., 1971, *Basic Lubrication Theory*, Ellis Horwood, London.
- [18] Feng, N. S., and Hahn, E. J., 1986, "Cavitation Effects on Squeeze-Film Damper Performance," *STLE Tribology Transactions*, 29 (3), pp. 353 - 360.
- [19] Munson, B. R., Young, D. F., and Okiishi, T. H., 1998, *Fundamentals of Fluid Mechanics*, John Wiley and Sons, New York.